SUPPLEMENTARY MATERIAL (SM1 & SM2)

Long-Term Cyclicities in Phanerozoic Sea-Level Sedimentary Record and Their Potential Drivers

Slah Boulila[a,b,1], Jacques Laskar[b], Bilal U. Haq[a,c], Bruno Galbrun[a], and Nathan Hara[b]

[a]Sorbonne Universités, UPMC Univ Paris 06, CNRS, Institut des Sciences de la Terre de Paris (ISTeP), 4 place Jussieu 75005 Paris, France; [b]Astronomie et Systèmes Dynamiques IMCCE, Observatoire de Paris, 77 Avenue Denfert-Rochereau, 75014 Paris, France; and [c] Smithsonian Institution, Washington DC, USA.

[1]Corresponding author. Tel: +33.144274163; Fax: +33.144273831. E-mail: slah.boulila@upmc.fr.

Supplementary material SM1

I. Supporting information on time-series analysis

Spectral analysis of both undetrended and detrended Phanerozoic eustatic data (Fig. S1a,b) shows two significant (>99% CL) peaks centered on ~36 and ~91 Myr A less significant (>95% CL) peak centered on ~9.3 Myr is also present. While the ~36 Myr cyclicity can be visually examined, neither the ~9.3 Myr nor the ~91 Myr are visually obvious. The ~9.3 Myr persists even when considering different timescales (Fig. S2). It may correspond to the shorter 2nd order eustatic sequences of Haq et al. (ref. 1) (i.e., their "*supersequences",* Fig. S3), which were shown to be quasi-periodic e.g., in the past ~70 Ma. A cyclicity of ~9 Myr period was highlighted, for the first time, in the Cenozoic carbon-cycle proxies (ref. 2).

To further pursue the ~91 Myr peak we performed spectral analysis per intervals and applied filtering. Spectra of both 0-251 Ma (Cenozoic-Mesozoic) and 251-542 Ma (Paleozoic) intervals (Fig. S1c,d) reveal the persistence of the ~36 Myr peak, however, the ~91 Myr is 98 Myr in the Ceno-Mesozoic and only 86 Myr in the Paleozoic. Bandpass filter output of the ~36 Myr cycle band points to the persistence of this cycle at least throughout the last 500 Ma (Fig. S3). This result is strongly supported by evolutive harmonic analysis (main Fig. 4). For the ~91 Myr 'unstable' peak, we applied filtering in two different ways, first to the whole (0-542 Ma) data, then, per intervals: the Ceno-Mesozoic (0-251 Ma) and the Paleozoic (251-542 Ma) intervals. Filtering the whole data is more conservative than that per intervals (filter-edge effects). Thus, we provide filter output of the whole data (Fig. S3) to interpret the two aforementioned peaks (~98 and ~86 Myr, Fig. DR1c,d). Ceno-Mesozoic filter output indicates that the ~98 Myr peak corresponds to the average of the two following bundlings: the three (C2-M1-M2) and the three (M3-M4-M5) ~36 Myr cycles (Fig. DR2). Paleozoic filter output points to the same conclusion (i.e., 36 Myr harmonics). The ~86 Myr peak equals to the average of the three following bundlings : the two (P1-P2), the two (P3-P4), and the three (P5-P6-P7) ~36 Myr cycles (Fig. S3). In summary, filtering shows that the ~91 Myr peak may originate from harmonics of the fundamental ~36 Myr cycle, as the average of two or three cycles. The unstationary of the ~91 Myr cycle could also be related to the length of the time series, which is too short to precisely detect such cyclicity. Despite the possibility that the ~91 Myr cycle could have a galactic (and thus climatic) significance, we will focus on the relatively well constrained ~36 Myr (see main text).

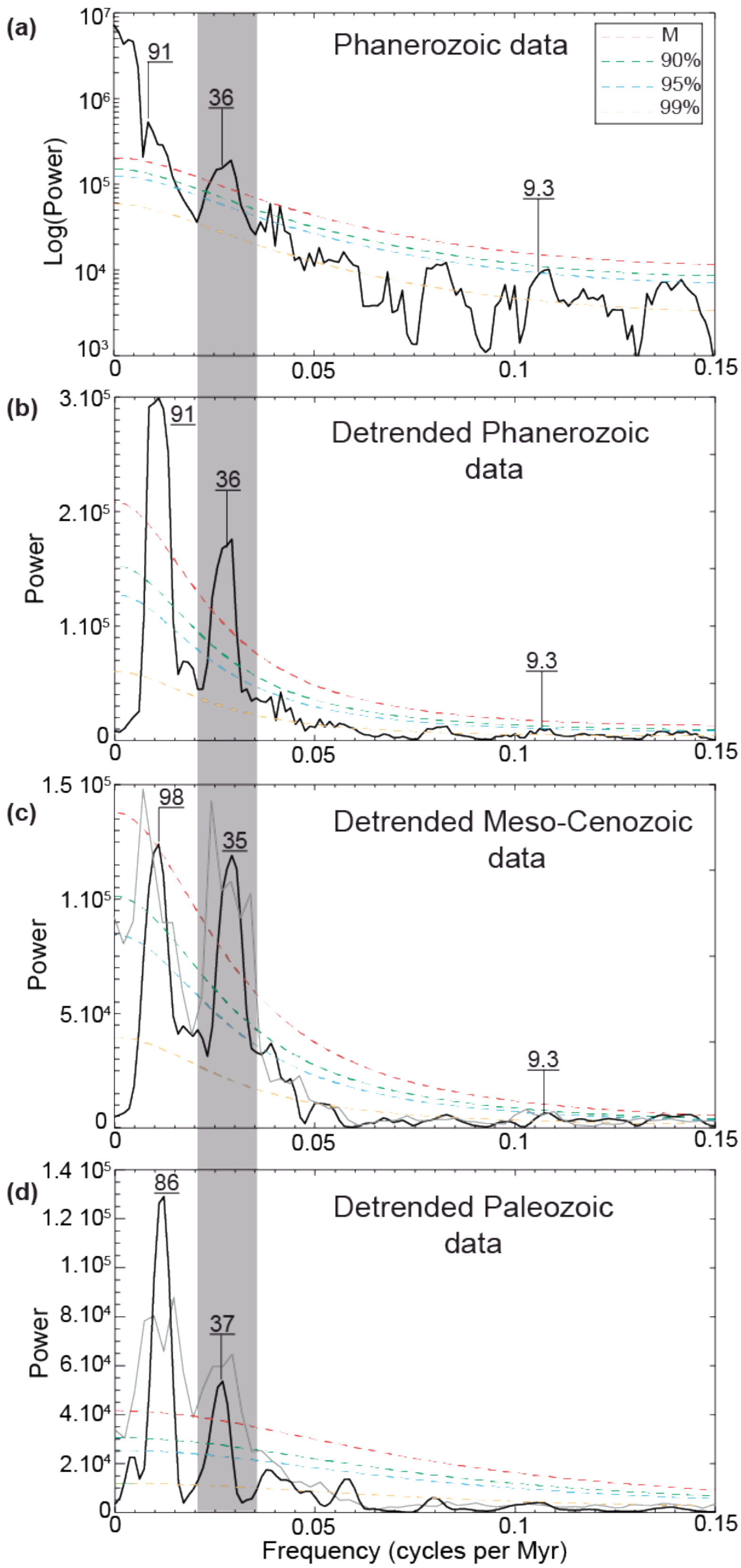

Figure S1: 2pi-MTM power spectra of the Phanerozoic eustatic (ref. 1,3,4). Results of noise modeling were estimated using linear fitting and median filtering over 20% of the Nyquist frequency. **(a)** The original whole (Phanerozoic) data (Fig. 1b in the main text). **(b)** The detrended whole data (Fig. 1d in the main text). **(c)** The detrended Cenozoic-Mesozoic (0-251 Ma) interval without (gray spectrum) and with (black spectrum) 1x-zero padding of the series. **(d)** The detrended Paleozoic (251-542 Ma) interval without (gray spectrum) and with (black spectrum) 1x-zero padding of the series. Zero-padding is used to precisely determine periods of spectral peaks. The ~36 Myr cyclicity depicted by the continuous spectral peak throughout the Phanerozoic Eon is shown by gray shaded area (see also evolutive harmonic analysis in main Fig. 4 for the continuity of the ~36 Myr cyclicity).

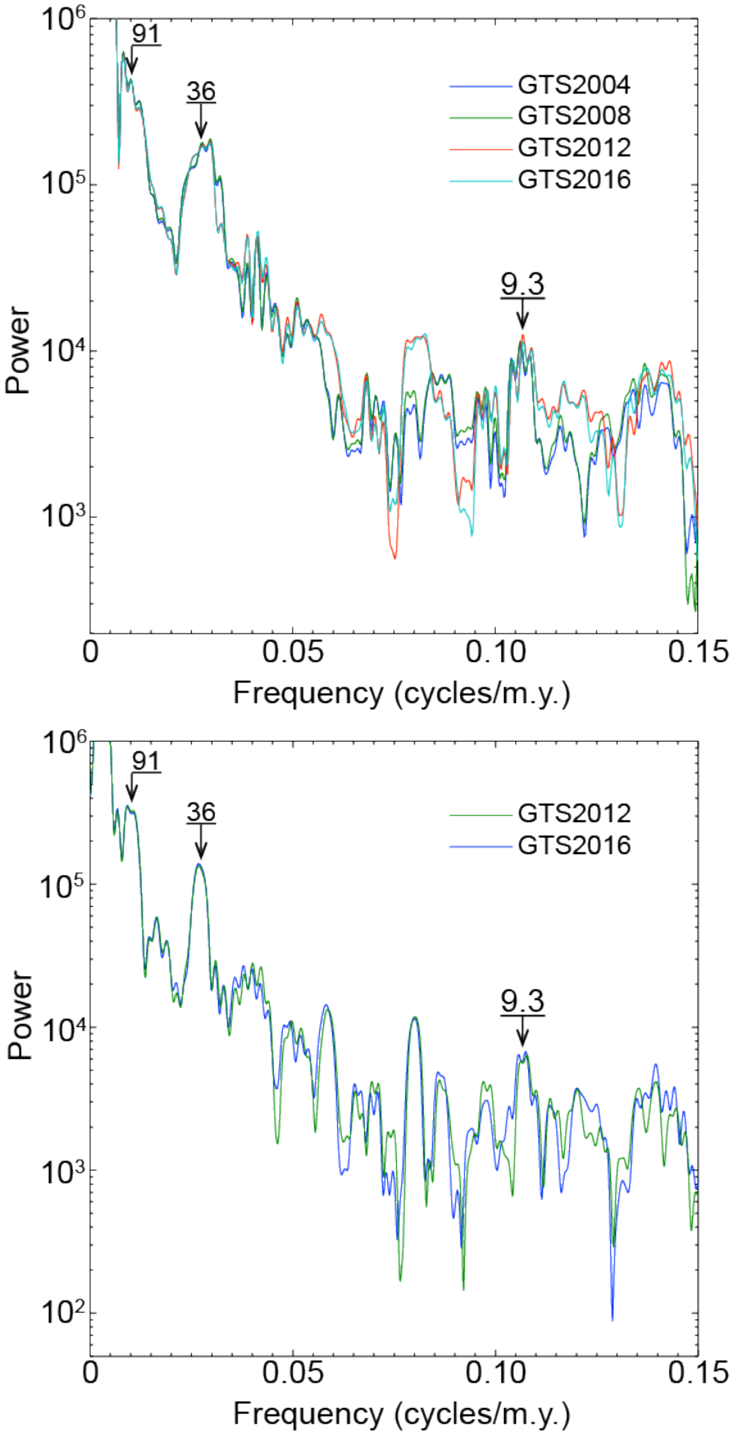

Figure S2: 2 π-MTM power spectra of the raw Phanerozoic eustatic data using different Geologic timescales GTS. Upper spectra: spectra without padding. Lower spectra: spectra of the 2x padded data. Note the persistence of the lower frequencies whatever the GTS version. We have also tested GTS2016 uncertainties on the lower frequencies using Markov Chain Monte Carlo (MCMC) Bchron simulations (see main Fig. 2).

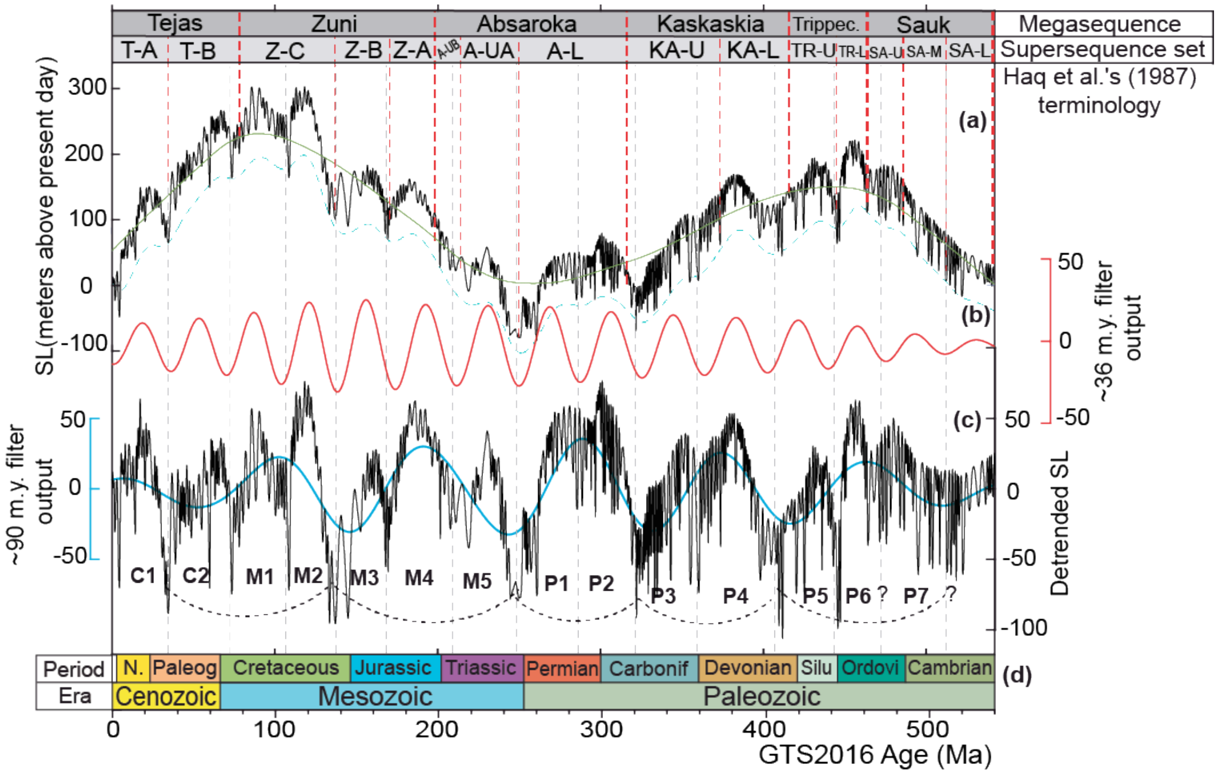

Figure S3: (a) Phanerozoic eustatic curve (ref. 1,3,4) with the fitted megacycles and Haq et al.'s (ref. 1) sequence definition and terminology. Vertical thick-dashed lines delimit megasequence boundaries, vertical thin-dashed lines delimit supersequence set boundaries. Supersequence sets are as follows. T-A and T-B: Tejas A and B. Z-C, Z-B and Z-A: Zini C, B and A. A-UB, A-UA and A-L: upper Absaroka B, upper Absaroka A, and lower Absaroka. KA-U and KA-L: upper Kaskaskia and lower Kaskaskia. TR-U and TR-L: upper Trippecanoe and lower Trippecanoe. SA-U, SA-M and SA-L: upper Sauk, middle Sauk, and lower Sauk. **(b)** Gaussian bandpass filter output (0.028 ± 0.012 my^{-1} frequency cutoff) to recover the ~36 Myr cycle. **(c)** Detrended eustatic curve: residuals of the 25% weighted average in 'a'; C1, C2, M1-M5, and P1-P7 are the ~36 Myr cycles (roughly 'C' for Cenozoic, 'M' for Mesozoic, and 'P' for Paleozoic), question marks indicate that ~36 Myr cycle boundaries are uncertain. Gaussian bandpass filter output (0.011 ±0.005 Myr^{-1} frequency cutoff) to recover the ~91 Myr cycle (in blue), the ~36 Myr cycle bundlings are also shown with arcs. **(d)** Geologic time scale 2016, GTS2016 (ref. 5), Period: white box, Quaternary, N.: Neogene, Paleog: Paleogene, Carbonif: Carboniferous, Silur: Silurian, Ordovic: Ordovician.

II. Very long-term eustatic cycles vs. other geologic process during the Phanerozoic Eon

Statistical significance and possible origin of multi-Myr cycles in geological records (e.g., biomass extinctions, climate change, Earth's interior dynamics, eustatic changes, etc) have been considered by several researchers since the 1980's (ref. 6-24, and many others).

In particular, a series of geologic events have been suggested to be related with a dominant ~30 ±5 Myr periodicity (e.g., ref. 10-13). The regularity, statistical significance, and origin of this dominant ~30 ±5 Myr periodicity have, however, been the subject of a long debate (e.g., ref. 6-8, 20, 25).

One hypothesis to explain biotic extinctions relates the cyclic variations to changes in the flux of the cosmic rays (CR) or of the Oort cloud comet, both in response to the Sun's oscillation about the galactic midplane (e.g., ref. 22, 24, 26).

In this study, we show that the most recent and revised Phanerozoic eustatic curve documents a prominent and continuous ~36 Myr cyclicity superimposed on Cenozoic-Mesozoic and Paleozoic megacycles (~250-Myr-long) (Fig. S4). These cyclicities were also suggested from several geological proxies (production rate on oceanic crust, temperature, biodiversity) (Fig. S4). Moreover, the most constrained deep-sea Cenozoic $\delta^{18}O$ data show the ~36 Myr cycle, matching well the eustatic cycle (Fig. 3 from the main text). The ~35 Myr Cenozoic $\delta^{18}O$ cycle was even previously recognized by Kaiho and Saito (ref. 13).

Our study outlines, for the first time, highly significant ~36 and ~250 Myr periodicities in a relatively well-constrained Phanerozoic sea-level record. Such periodicities are *à priori* astronomically predicated. The ~36 Myr period is equivalent to half-period of solar-system vertical motion. The ~250 Myr period could correspond to a period of radial solar-system motion (see SM2). This intriguing correspondence may hint at a possible connection between astronomy and geology. We then build a CR model that takes into account vertical and radial motions of the solar system in the galaxy, and may explain longer-term glacioeustatically driven SL changes (see SM2).

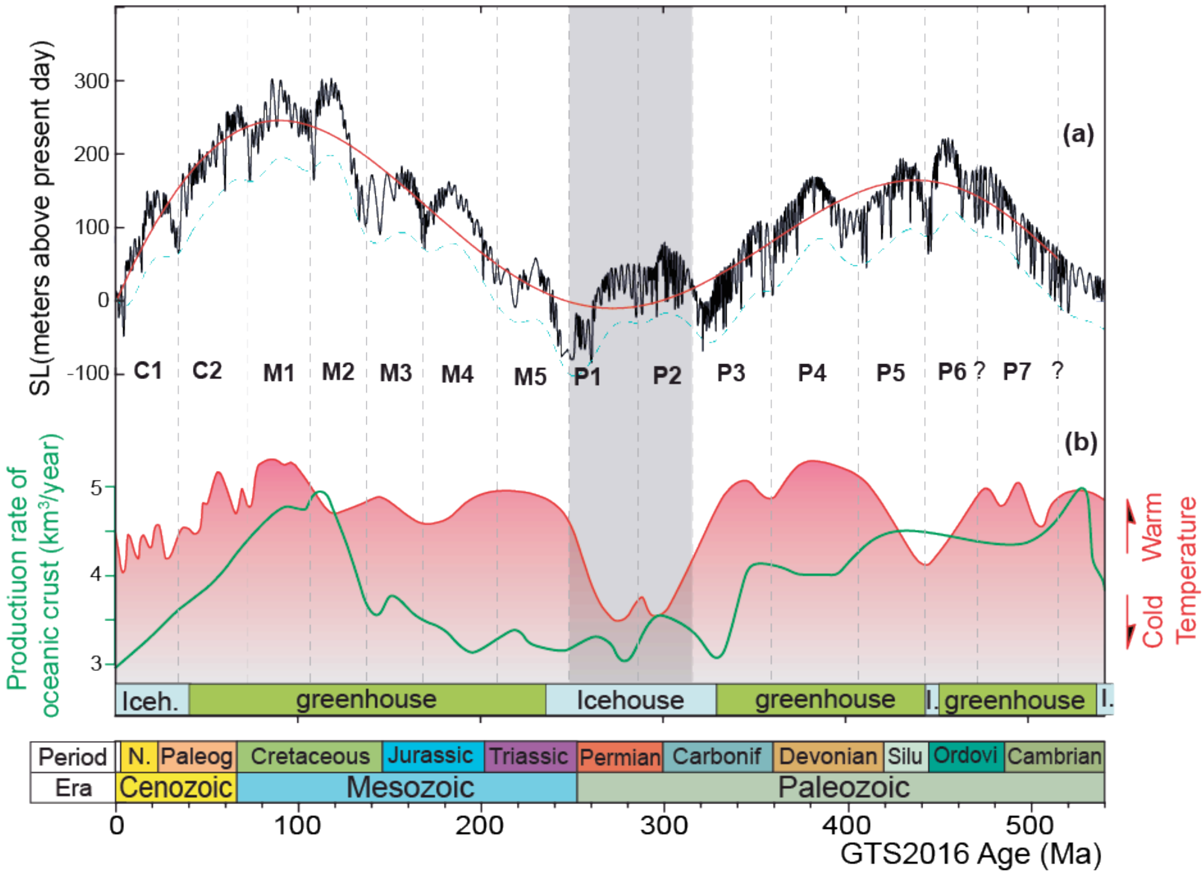

Figure S4: Comparison of the Phanerozoic eustatic variations with other geologic events. **(a)** Original Phanerozoic eustatic curve (ref. 1, 3). Cenozoic-Mesozoic and Paleozoic megacycles are fitted with six-order polynomial method (green curve). Lowpass Gaussian filtering (blue curve) highlights both ~36 Myr cycles (labelled as in Fig. 1b in the main text) and megacycles. **(b)** Oceanic crust production rates (green curve) are from Stanley (ref. 29), temperature variations (red curve) are from Frakes et al. (ref. 30), and climate model (icehouse vs greenhouse periods) is from Frakes et al. (ref. 30) where Cenozoic icehouse period is updated according to Zachos et al. (ref. 27, 28), grey-shaded 'P1' and 'P2' indicate a possible node (minimum) in the megacycle variations.

III. Supporting information on Phanerozoic $\delta^{18}O$ data

A recent study of Shaviv et al. (2014) (ref. 31) have used $\delta^{18}O$ data from specific fossils to conclude the persistence of the 32 Myr cyclicity throughout the Phanerozoic eon. In particular, they have used two $\delta^{18}O$ compilations: (1) $\delta^{18}O$ "ML200" compilation is considered as the "master" record used to highlight the 32 Myr cyclicity, and (2) $\delta^{18}O$ "ML175" compilation, which is close to ML200 but reduce jump between datasets). Both compilations do not include Cenozoic deep-sea $\delta^{18}O$ data, while those data show evidence of the 35 Myr cyclicity (Fig. S5). Here, we show that the temporally most constrained 0-65 Ma interval (Cenozoic) from their both (raw) compilations ML200 and ML175 does not show obvious 32 Myr cycles (Fig. S5). Instead, we argued (as in the main text, see main Fig. 5) that deep-sea (benthic foraminifera) composite $\delta^{18}O$ curve (e.g., ref. 27, 28) detects faithfully the ~32 Myr cyclicity (Fig. S6), pointing to glacio-eustatically driven SL change.

Accordingly, we have compiled $\delta^{18}O$ data as follows. We focused on the past 202 Ma interval because, with the exception of the interval around 120 Ma, (i) it includes high resolution data, (ii) it represents less $\delta^{18}O$ amplitude fluctuations (less scatter), and (iii) it possesses less significant observational gaps. For the interval 0–112 Ma, we used only the high-resolution deep-sea (benthic foraminifera) data (ref. 27, 28, 32 and 33). For the interval 112–202 Ma, we used only $\delta^{18}O$ data from brachiopods and belemnites (ref. 34) to reduce differential effects from fossil groups on $\delta^{18}O$ values. The resulting (202-Myr-long) compiled $\delta^{18}O$ signal is then calibrated to the recent geologic time scale GTS2016 (Fig. S7).

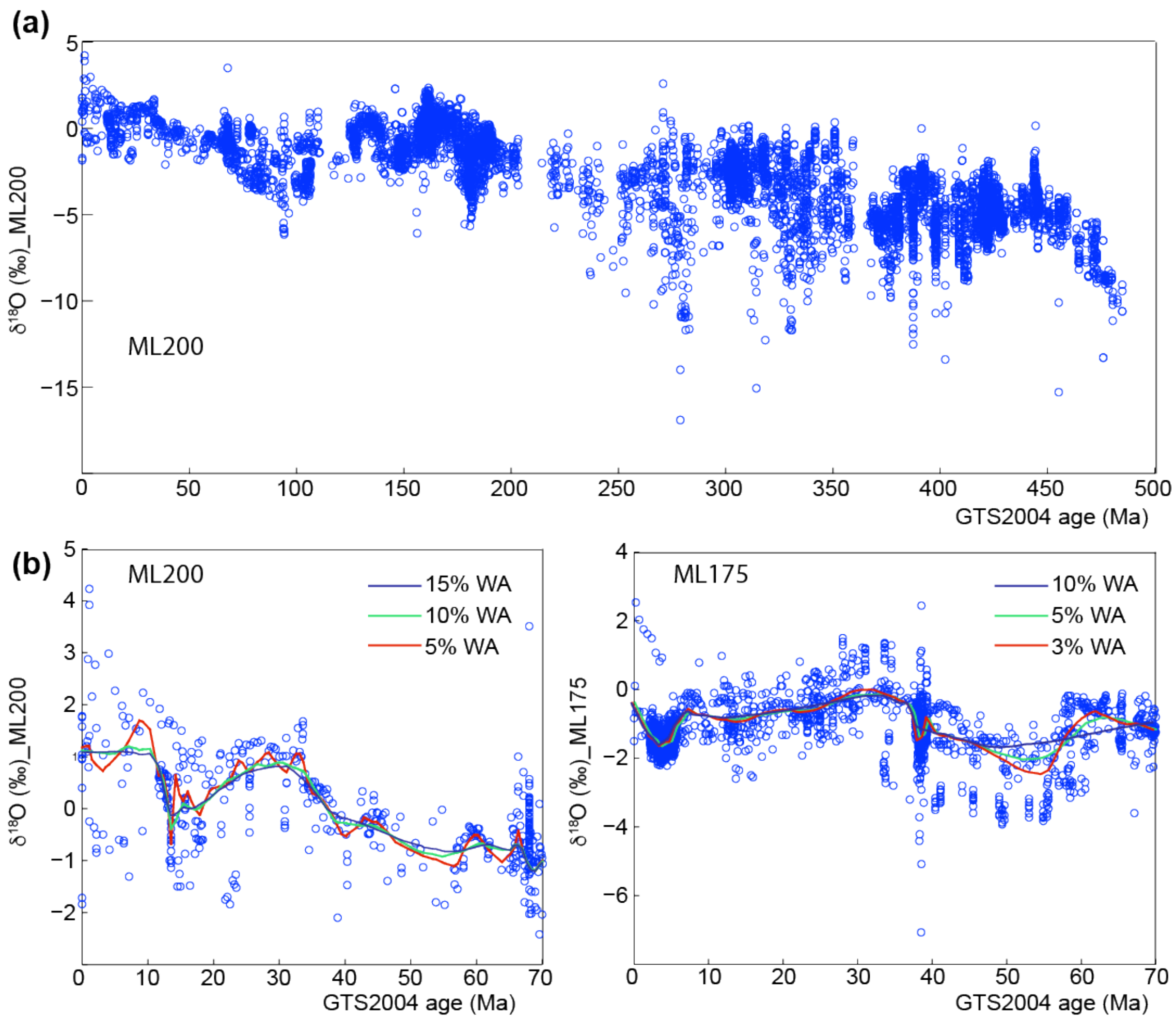

Figure S5: Phanerozoic $\delta^{18}O$ data (ref. 31). **(A)** $\delta^{18}O$ data for the interval 0-490 Ma. **(B)** $\delta^{18}O$ data for the interval 0-70 Ma from ML200 compilation (left panel), and ML75 compilation (right panel). Weighted Averages (WA) are applied using different smoothing factors (15%WA, 10%WA, 5%WA and

3%WA). Note that there is no clear cyclicity at 32 Myr band neither in ML200 nor in ML175 compilations in the Cenozoic interval.

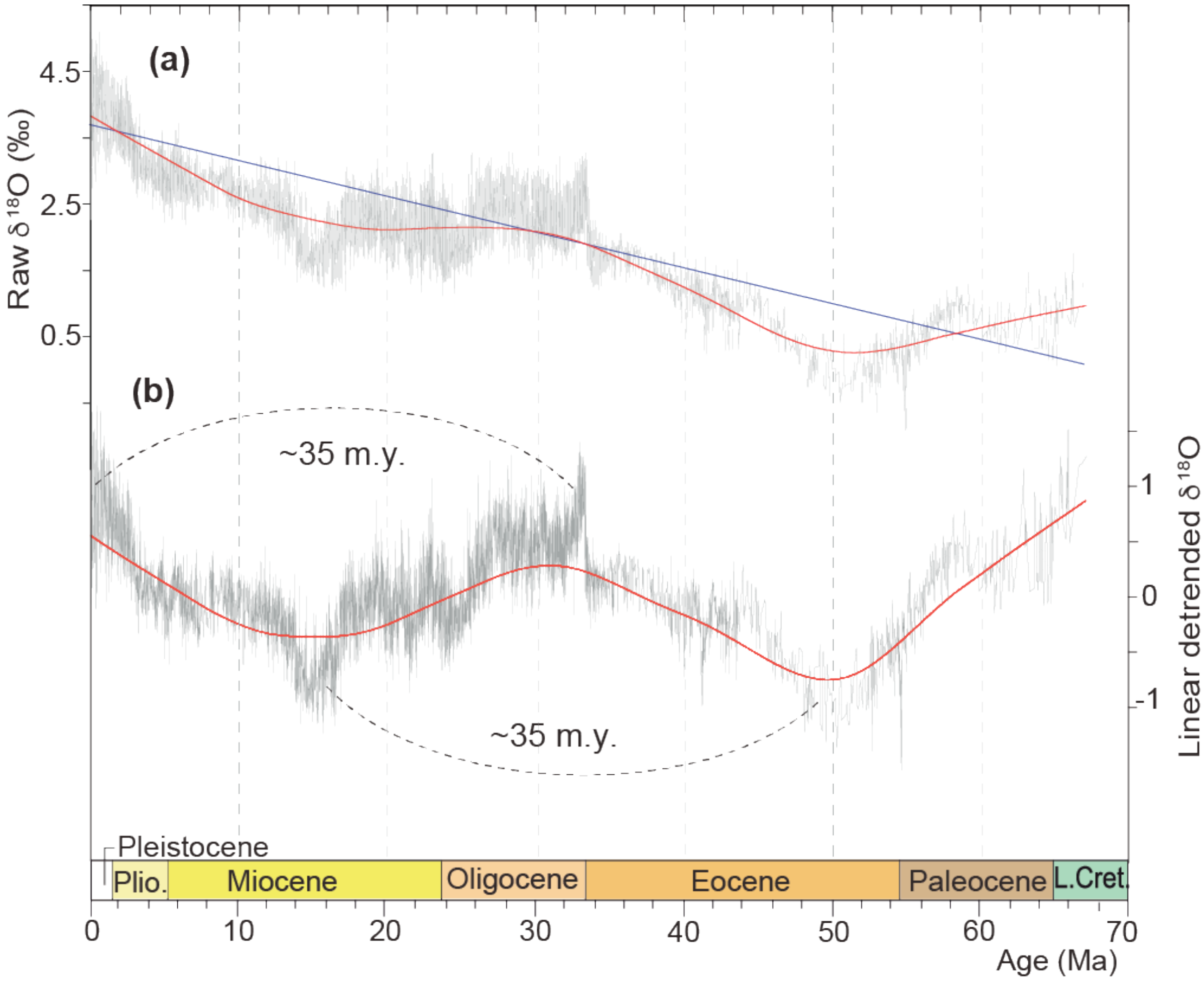

Figure S6: Strong ~35 Myr cyclicity in the Cenozoic $\delta^{18}O$ data. **(a)** Raw benthic foraminiferal oxygen isotopes $\delta^{18}O$ (ref. 27, 28), linear trend and a 25% weighted average of the series are also shown. **(b)** Linear-detrended $\delta^{18}O$, a 25% weighted average of the linear-detrended series and the strong ~35 Myr cycle are shown.

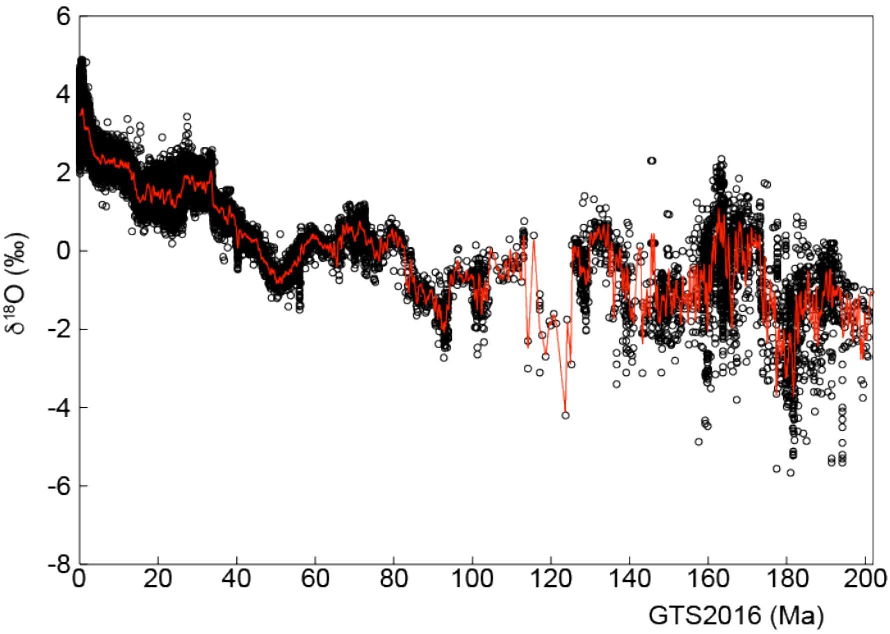

Figure S7: $\delta^{18}O$ data over the past 202 Ma (ref. 32,33,34) calibrated to the Geologic Time Scale 2016, GTS2016 (see text for details about compilation). The red curve is the fitted data using the least-square method.

REFERENCES CITED

1. Haq BU, Hardenbol J, Vail PR (1987) Chronology of fluctuating sea levels since the Triassic. Science 235:1156–1167.
2. Boulila, S., Galbrun, B., Laskar, J., and Pälike, H., 2012, A ~9 myr cycle in Cenozoic $\delta^{13}C$ record and long-term orbital eccentricity modulation: Is there a link?: Earth Planet Sci. Lett., v. 317–318, p. 273–281.
3. Haq BU, Al-Qahtani AM (2005) Phanerozoic cycles of sea-level change on the Arabian Platform. GeoArabia 10:127–160.
4. Haq BU, Schutter SR (2008) A chronology of Phanerozoic Sea-Level Changes. Science 322:64–68.
5. Ogg, J.G., Ogg, G., and Gradstein, F.M. (2016) A Concise Geologic Time Scale 2016: Elsevier, store.elsevier.com/9780444637710, 234 p.
6. Raup DM, Sepkoski JJJr (1984) Periodicity of extinctions in the geologic past. Proc. Nat. Acad. Sci. USA 81:801-805.
7. Raup DM, Sepkoski JJJr (1988). Testing for periodicity of extinction. Science 241:94-96.
8. Rampino MR, Stothers RB (1984) Geological rhythms and cometary impacts. Science 226:142–143.
9. Rampino MR, Stothers RB (1988) Flood basalt volcanism during the past 250 million years. Science 241:663–668.
10. Rich JE, Johnson GL, Jones JE, Campsie J (1986) A significant correlation between fluctuations in seafloor spreading rates and evolutionary pulsations. Paleoceanography 1:85–95.
11. Negi JG, Tiwari RK, Rao KNN (1990) 'Clean' spectral analysis of long-term sea-level changes.

Terra Nova 2:138–141.
12. Rampino RM, Caldeira K (1993) Major episodes of geologic change: correlations, time structure and possible causes. Earth Planet Sci Lett 114:215–227.
13. Kaiho K, Saito S (1994) Oceanic crust production and climate during the last 100 Ma. Terra Nova 6:376–384.
14. Hallam A, Wignall PB (1999) Mass extinctions and sea-level changes. Earth Sci Rev 48:217–250.
15. Prokoph A, Rampino MR, Bilali H (2004) Periodic components in the diversity of calcareous plankton and geological events over the past 230 my. Palaeogr Palaeoclim Palaeoecol 207:105–125.
16. Prokoph A, Shields GA, Veizer J (2008) Compilation and time-series analysis of a marine δ18O, δ13C, 87Sr/86Sr and δ34S database through Earth history. Earth Sci Rev 87:113–133.
17. Rohde RA, Muller RA (2005) Cycles in fossil diversity. Nature 434:208–210.
18. Omerbashich M (2006) A Gauss-Vanícek Spectral Analysis of the Sepkoski Compendium : No New Life Cycles. Comput Sci Engineer 9:26-30.
19. Cornette JL (2007) Gauss-Vaníček and Fourier Transform Spectral Analyses of Marine Diversity. Comput Sci Engineer 9:62, doi: 10.1109/MCSE.2007.76
20. Lieberman BS, Melott AL (2007) Considering the Case for Biodiversity Cycles: Reexamining the Evidence for Periodicity in the Fossil Record. PLoS One 2(8):e759 doi:10.1371/journal.pone.0000759.
21. Alroy J, et al. (2008) Phanerozoic Trends in the Global Diversity of Marine Invertebrates. Science 312:97–100.
22. Melott AL (2008) Long-term cycles in the history of life: Periodic biodiversity in the Paleobiology Database. PloS One 3(12):e4044. doi:10.1371/journal.pone.0004044
23. Bailer-Jones CAL (2009) The evidence for and against astronomical impacts on climate change and mass extinctions: A review. Int J Astrob 8:213–239.
24. Melott AL, Bambach RK (2011) An ubiquitous ~62 my periodic fluctuation superimposed on general trends in fossil biodiversity: Part I, Documentation. Paleobiology 37:92-112.
25. Sepkoski JJJr (1989) Periodicity in extinction and the problem of catastrophism in the history of life. J Geol Soc London 146:7–19.
26. Matese JJ, Whitman PG, Innanen KA, Valtonen MJ (1995) Periodic Modulation of the Oort Cloud Comet Flux by the Adiabatically Changing Galactic Tide. Icarus 116:255–268.
27. Zachos JC, Dickens GR, Zeebe RE (2008) An early Cenozoic perspective on greenhouse warming and carbon-cycle dynamics. Nature 451:279–283.
28. Zachos JC, Pagani M, Sloan L, Thomas E, Billups K (2001) Trends, Rhythms, Aberrations in Global Climate 65 Ma to Present. Science 292:686–693.
29. Stanley SM (1999) Earth System Histrory. WH Freeman and Company, New York, 615 p.
30. Frakes LA, Francis JE, Syktus JI (1992) Climate Modes of the Phanerozoic: The History of the Earth's Climate Over the Past 600 Million Years. Cambridge University Press 274 p.
31. Shaviv, N.J., Prokoph, A., and Veizer, J., 2014, Is the Solar System's Galactic Motion Imprinted in the Phanerozoic Climate?: Scientific Reports, v. 4, no. 6150, doi:10.1038/srep06150.

32. Cramer, B.S., Toggweiler, J.R., Wright, J.D., Katz, M.E., and Miller, K.G., 2009, Ocean overturning since the Late Cretaceous: Inferences from a new benthic foraminiferal isotope compilation. Paleoceanography, v. 24, PA4216, doi: 10.1029/2008PA001683.

33. Friedrich, O., Norris, R.D., and Erbacher, J., 2012, Evolution of middle to Late Cretaceous oceans—A 55 m.y. record of Earth's temperature and carbon cycle. Geology, v. 40, p. 107–110.

34. Veizer, J., and Prokoph, A., 2015, Temperatures and oxygen isotopic composition of Phanerozoic oceans: Earth-Science Reviews, v. 146, P. 92–104.

Supplementary material SM2

Supplementary Information (2)
Galactic trajectories and cosmic rays

1 Models

The precise form of the galactic potential is still largely unknown. A variety of models exists in the literature (see Binney and Tremaine, 2008), but despite improvements in the constraints resulting from Hipparchos data, strong constraints are still missing (Dehnen and Binney, 1998). Because of the lack of constraints, we choose to use a model for the galactic potential that is as simple as possible, derived from the one of (Paczynski, 1990). This model comprises a bulge, a disk and a halo.

The bulge and disk of mass M_1 and M_2 are given by Miyamoto and Nagai potential Φ_1 and Φ_2 of the form (Miyamoto and Nagai, 1975)

$$\Phi_i(r,z) = -\frac{GM_i}{(r^2 + \left[a_i + (z^2+b_i^2)^{1/2}\right]^2)^{1/2}}$$

with associated density

$$\rho_i(r,z) = \frac{b_i^2 M}{4\pi} \frac{a_i r^2 + (a_i + 3(z^2+b_i^2)^{1/2})(a_i + (z^2+b_i^2)^{1/2})^2}{(r^2 + (a_i + (z^2+b_i^2)^{1/2})^2)^{5/2}(z^2+b_i^2)^{3/2}} \ .$$

The potential of the Halo component is (Paczynski, 1990)

$$\Phi_h = \frac{GM_h}{h}\left[\frac{1}{2}\log\left(1+\frac{R^2}{h^2}\right) + \frac{h}{R}\arctan(\frac{R}{h})\right] \ .$$

with $R = \sqrt{r^2+z^2}$ and associated density

$$\rho_h = \frac{M_h}{4\pi h(R^2+h^2)} \ .$$

The total potential is $\Phi = \Phi_1 + \Phi_2 + \Phi_h$. The equations of motion will be

$$\begin{aligned} \ddot{r} - r\dot{\phi}^2 &= -\frac{\partial\Phi}{\partial r} \\ \frac{d}{dt}(r^2\dot{\phi}) &= -\frac{\partial\Phi}{\partial\phi} = 0 \\ \ddot{z} &= -\frac{\partial\Phi}{\partial z} \end{aligned}$$

Due to rotational symmetry, we have $r^2\dot{\phi} = C$ constant (angular momentum conservation). We have also the conservation of the total energy per unit mass ($dH/dt = 0$) with

$$H = \frac{1}{2}(\dot{r}^2 + r^2\dot{\phi}^2 + \dot{z}^2) + \Phi(r, z) \ .$$

The system can thus be reduced to a system of order 4, but we prefer to use a phase space of dimension 5 with the integral of the energy as a verification for the accuracy of the integration. We use the set of variables (r, ϕ, z, p_r, p_z) with $p_r = \dot{r}$, $p_z = \dot{z}$ and the system of equations of first order

$$\begin{aligned} \dot{r} &= p_r \\ \dot{\phi} &= \frac{C}{r^2} \\ \dot{z} &= p_z \\ \dot{p_r} &= -\frac{\partial\Phi}{\partial r} + \frac{C^2}{r^3} \\ \dot{p_z} &= -\frac{\partial\Phi}{\partial z} \end{aligned} \tag{1}$$

2 Parameters and initial conditions

The initial conditions for the Sun (Binney et al., 1997; Reed, 2006; Schönrich et al., 2010) are given in Table 1. The constraint on the longitudinal velocity of the Sun is (Reid and Brunthaler, 2004).

Table 1: Initial conditions.

r_0	8300 pc ± 300
z_0	14 pc ± 4
ϕ_0	0
$\dot{r}_0$	-11 km/s ± 1
$\dot{z}_0$	7 km/s ± 0.5

$$v_0 = r_0\dot{\phi}_0 = 236 \pm 15 km/s$$

which provides the value of $C = r_0^2\dot{\phi}_0 = r_0 v_0$. The gravitational constant G, expressed in pc and Myr is $G = 0.0044755$ (equivalent to 4.302×10^{-3} pc $M_\odot^{-1}$ (km/s)^2 with 1 pc/Myr=0.98 km/s).

2.1 Parameters

For our model, we have chosen parameters that are slightly different from the ones of (Paczynski, 1990) (Table 2). To determined these parameters, we iterated some fitting process in order to retrieve as close as possible the features observed in the geological data, keeping the initial conditions that are provided by stellar data (Table 1). This model can be though as a galactic model that is both fitted to stellar data and to geological data. It departs slightly from conventionally adopted galactic models as (Paczynski, 1990), but is still fully compatible with the up to date observational data (Table 1) (Schönrich et al., 2010).

Table 2: Parameters of the potential. P90 design the parameters from the model of (Paczynski, 1990)

	P90	This study
M_1	1.12 E10 $M_\odot$	2.3 E10 $M_\odot$
a_1	0	0
b_1	277 pc	277 pc
M_2	8.07 E10 $M_\odot$	9.5E10 $M_\odot$
a_2	3700 pc	4600 pc
b_2	200 pc	193 pc
M_h	5. E10 $M_\odot$	5. E10 $M_\odot$
h	6000 pc	24 600 pc

With this set of parameters, we obtain a stellar density in the vicinity of the Sun of $0.213 M_\odot/\mathrm{pc}^3$ which is slightly larger than the value $0.158 M_\odot/\mathrm{pc}^3$ of (Paczynski, 1990).

2.2 Numerical integration

The equations of motions are integrated using a Runge-Kutta method of order 8/7 (Hairer et al., 1993). The maximum variation of the relative energy smaller than 3.5×10^{-15} over 2 Gyr. The orbit present vertical and radial oscillations with respective periods 72 and 254 Myr (Figs.1,2).

3 Cosmic Rays

Primary cosmic rays, up to a few Tev are created by violent phenomena in the galaxy, as explosions of stars, that can be traced by supernovae remnants and pulsars (see Delahaye, 2010). The distribution of these potential sources of cosmic rays in the Milky Way can be modelized by an expression of the form

$$\rho(r, z) = \rho_0 r^a \exp\left(-\frac{r}{r_0}\right) \exp\left(-\frac{|z|}{z_0}\right) \ . \tag{2}$$

Although this general expression is in agreement with the observational results, some large uncertainty remains for the determination of the parameters in this expression (see Delahaye, 2010). Here we are mostly interested in the qualitative aspect of this distribution, and we have chosen the set of parameters L04 from (Lorimer, 2004) with $a = 2.35$, $r_0 = 1528$ pc, and $z_0 = 100$ pc (as in (Delahaye, 2010)). The expression (2) provides the distribution

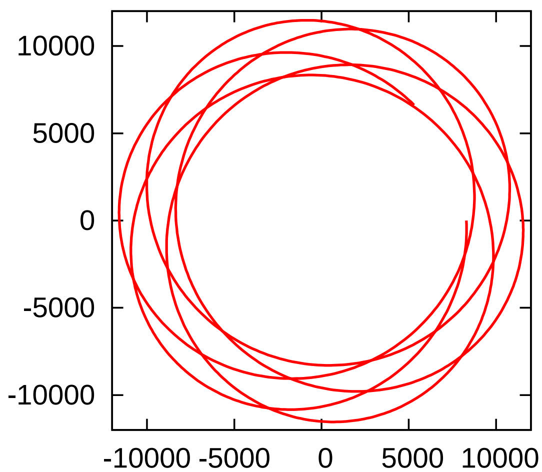

Figure 1: Projection of the orbit of the Sun in the galactic plane over 1.5 Gyr in the past. Units are in parsecs (pc).

of the cosmic rays sources, but we are interested in the distribution of the cosmic rays in the Milky Way, and more particularly in the vicinity of the Solar orbit. Ideally, we would need to make some model for cosmic rays propagation, which is an involved process which relies on many unknown parameters (see Delahaye, 2010). On the other hand, the resulting distribution of cosmic rays, as depicted for example by the figure 7.2 of (Delahaye, 2010) seems to rely on simple smooth functions, that could thus be obtain by relatively simple reasoning.

3.1 Distribution of cosmic rays in the Milky Way

In order to have a qualitative model for the distribution of cosmic rays, we simply assume that the cosmic rays propagation decreases as the inverse of the square of the distance from the source, as for any beam isotrope propagation. When limited to the galactic plane ($z = 0$), the flux at distance x from the galactic center will then be

$$\gamma_r(x) = \int_0^{+\infty} \rho_r(r) \frac{1}{|x-z|^c} dr \tag{3}$$

where $\rho_r(r) = \rho(r, 0)$ in (2) and $c = 2$. This function is then normalized such that $\gamma_r(r_0) = 1$. Using the L04 set of parameters for the sources, we obtain the distribution of cosmic rays given in Figure 3 (in red). In a similar way, the distribution in z is obtained as

$$\gamma_z(x) = \int_0^{+\infty} \rho_z(z) \frac{1}{|x-z|^c} dz \tag{4}$$

where $\rho_z(z) = \rho(r_0, z)$ in (2) and $c = 2$. The resulting distribution is given in Figure 4 (in red). As the hypothesis of isotropic distribution of the beam is an extreme case, we have

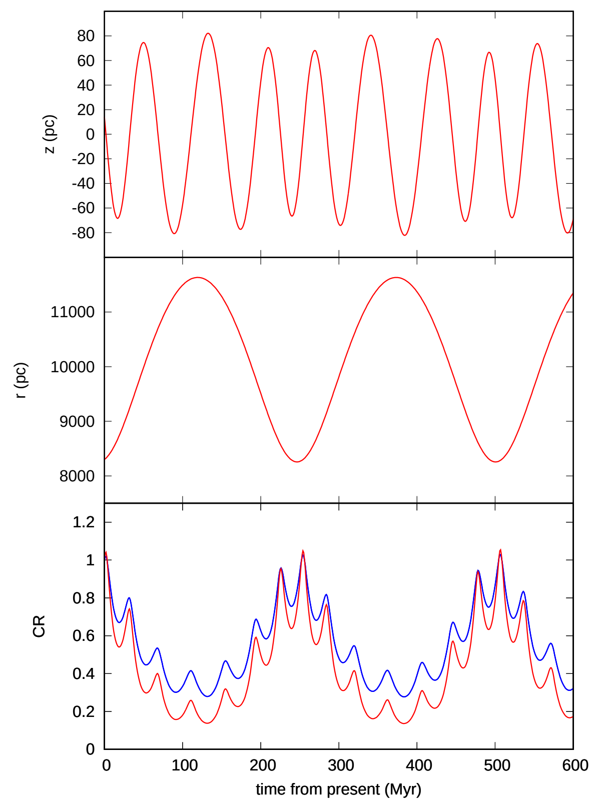

Figure 2: Top : variation of the vertical component (z in pc) of the Sun with respect to the galactic plane over 600 Myr in the past. Middle : Radial distance (r in pc) from the galactic center. Bottom : estimate of the variation of the cosmic ray flux on Earth resulting from the trajectory of the Sun in the Galaxy over 600 Myr in the past. In red with a decay in $1/d^2$, in blue with a decay in $1/d$.

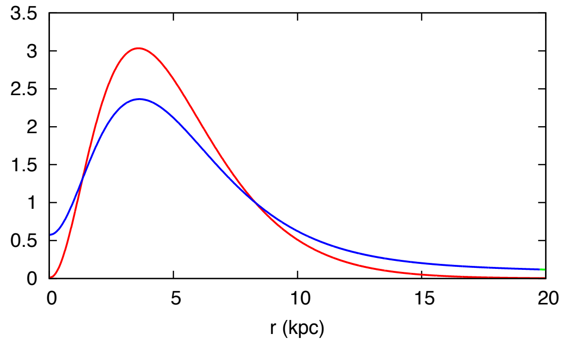

Figure 3: Distribution of cosmic rays as a function of r (in pc) obtained with the L04 distribution of sources and the model of propagation (3). The distribution is normalized in such way that it is equal to unity for the present location of the Sun ($r_0 = 8300$ pc). Red : decay in $1/d^2$. Blue : decay in $1/d$.

also considered the case when the beam is confined in the galactic disk. In this case, the law of propagation is given by (3, 4), but with $c = 1$. The corresponding curves are displayed in blue in figures 3, 4.

3.2 Adjusted laws

To make it more easy to handle, models are now fitted to the previous results in order to obtain analytical expressions for the rate of cosmic rays in the galaxy. We thus fit simple models to the previous results. For the evaluation in the z dirction, we limit ourselves to 100 pc, which is larger than the excursion of the Sun. We can thus use a simple model of the form

$$\tilde{\gamma}_z(z) = \exp\left(a_1\,|z| + a_2\,|z|^2 + a_3\,|z|^3 + a_4\,|z|^4 + a_5\,|z|^5\right) \tag{5}$$

that fits very well the numerical data obtained by solving the propagation law (4) (see Fig. 5). The coefficients a_i for the $1/d$ and $1/d^2$ models are provides in Table 3.

Table 3: Coefficient of the approximated formula (5) for the $1/d$ and $1/d^2$ models

	$1/d$	$1/d^2$
a_1	$+1.3330E-04$	$+4.8829E-05$
a_2	$-1.7432E-04$	$-3.2842E-04$
a_3	$+2.6428E-06$	$+5.8540E-06$
a_4	$-2.0977E-08$	$-5.0908E-08$
a_5	$+6.6520E-11$	$+1.7015E-10$

For the distribution in r, as the resulting law is more complex when the decay is in $1/d$, we choose to approximate the distribution in the [5 : 15] kpc range with a polynomial of

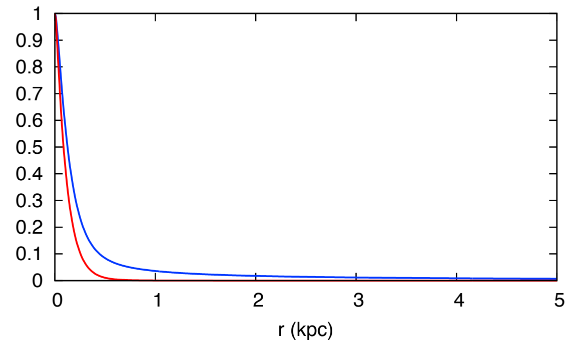

Figure 4: Distribution of cosmic rays as a function of z (in pc) obtained with the L04 distribution of sources and the model of propagation (3). The distribution is normalized in such way that it is equal to unity for the present location of the Sun ($z_0 = 14$ pc). Red : decay in $1/d^2$. Blue : decay in $1/d$.

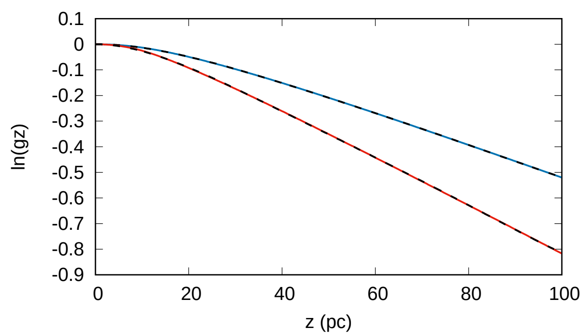

Figure 5: Distribution of cosmic rays as a function of z (in pc) obtained with the L04 distribution of sources and the model of propagation (3). In red : decay in $1/d^2$. In blue : decay in $1/d$. In both cases, the solid line is the numerical computation from the model $\gamma_z(z)$ 4, while the dotted line is the fitted model $\tilde{\gamma}_z(z)$ (4).

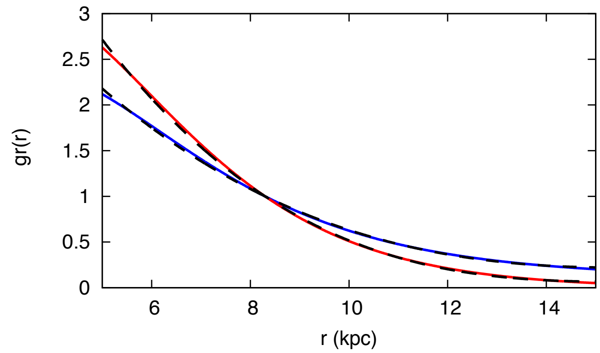

Figure 6: Distribution of cosmic rays as a function of r (in kpc) obtained with the L04 distribution of sources and the model of propagation (3). After polynomial fit of degree 3 $\tilde{\gamma}_r(r_0) = 1$. Red : decay in $1/d^2$. Blue : decay in $1/d$. In both cases, the solid line is the numerical computation from the models (3,4), while the black dotted line is the polynomial fit $\tilde{\gamma}_r(r)$ (6,7).

degree 3, with $\tilde{\gamma}_r(r_0) = 1$, as this is all we need for the evaluation of cosmic rays intensity in the vicinity of the Sun orbit. We thus obtain

$$\tilde{\gamma}_r(r) = 1 - 2.60 \times 10^{-04}(r - r_0) + 2.68 \times 10^{-08}(r - r_0)^2 - 7.94 \times 10^{-13}(r - r_0)^3 \tag{6}$$

for the decay law in $1/d$, and

$$\tilde{\gamma}_r(r) = 1 - 3.54 \times 10^{-04}(r - r_0) + 4.41 \times 10^{-08}(r - r_0)^2 - 1.80 \times 10^{-12}(r - r_0)^3 \ , \tag{7}$$

where r is in pc, for the decay in $1/d^2$ (Fig.6).

It should be noted that both vertical and radial distributions are is good agreement with the latest observational results from (Abdo et al., 2008; Ackermann et al., 2012; Abramowski et al., 2014; Bartoli et al., 2015; Chen et al., 2015; Acero et al., 2016).

The evolution of the orbit of the Sun in the Galaxy is then obtained by integrating the equations of motion (1), and the cosmic rays flux on the Solar System through time is obtained using the analytical approximate formula $\tilde{\gamma}_r(r)$ and $\tilde{\gamma}_z(z)$ with a total flux

$$\tilde{\gamma}(r, z) = \tilde{\gamma}_r(r)\tilde{\gamma}_z(z) \ . \tag{8}$$

The computed flux is given in Fig.2 (bottom) for the decay law in $1/d^2$ (in red) and the decay law in $1/d$ (in blue). It can be seen that the results do not differ much when we change the law of propagation of the cosmic rays in the Galaxy. Either curve can thus be used. We provide also in Fig.7 the evolution of the cosmic rays flux when only the vertical component of the motion (in z) is considered.

3.3 Discussion

In this study, we have used a potential for the Milky way with a rotational symmetry, as well as the distribution of cosmic rays sources. We have shown that a ~ 250 Myr periodicity

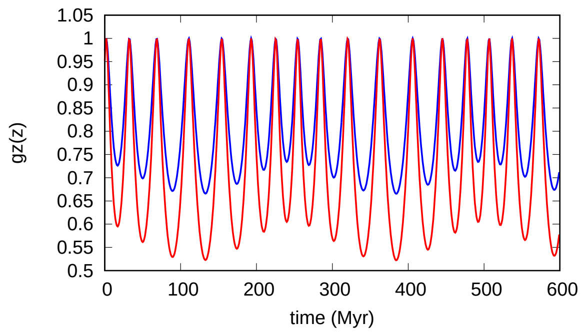

Figure 7: Distribution of cosmic rays as a function of time (in Myr in the past) obtained with the L04 distribution of sources and the model of propagation (3). only the vertical component $\tilde{\gamma}_z(z)$ of the motion is considered.

can be retrieved in the rate of cosmic rays on the Solar System by considering the radial excursion of the Sun. It should be noted that although the 72 Myr vertical period is very robust, the obtention of the 250 Myr period through radial variation of the Sun orbit requires some fine tuning that is made possible by the uncertainty that remains at present on the knowledge of the vicinity of the Sun and structure of the Milky way. With the future results of the GAIA astrometric mission, this uncertainty should be highly reduced.

If the derivation of the 250 Myr radial period is still possible, the present study would then provide an additional important constraint on the structure of the Milky way. If on the contrary the new Gaia data rule out the possibility of a 250 Myr radial period, one would have to search again for a possible explanation of the observation of this signature in the geological record as the possible time scale for the passage of the Sun through the spiral arms of the galaxy (Shaviv, 2002; Gies and Helsel, 2005; Svensmark, 2006), assuming that Gaia data will also constraint much better the structure of the spirals arms in the galaxy.

References

A. A. Abdo, et al. A Measurement of the Spatial Distribution of Diffuse TeV Gamma-Ray Emission from the Galactic Plane with Milagro. The Astrophysical Journal, 688: 1078–1083, December 2008. ISSN 0004-637X. Doi: 10.1086/592213.

A. Abramowski, et al. Diffuse Galactic gamma-ray emission with H.E.S.S. Physical Review D, 90: 122007, December 2014. ISSN 0556-2821. doi: 10.1103/PhysRevD.90.122007.

F. Acero, et al. Development of the Model of Galactic Interstellar Emission for Standard Point-source Analysis of Fermi Large Area Telescope Data. The Astrophysical Journal Supplement Series, 223:26, April 2016. ISSN 0067-0049. doi: 10.3847/0067-0049/223/2/26.

M. Ackermann, et al. Fermi-LAT Observations of the Diffuse -Ray Emission: Implications for Cosmic Rays and the Interstellar Medium. The Astrophysical Journal, 750:3, May 2012. ISSN 0004-637X. doi: 10.1088/0004-637X/750/1/3.

B. Bartoli, et al. Study of the Diffuse Gamma-Ray Emission from the Galactic Plane with ARGO-YBJ. The Astrophysical Journal, 806:20, June 2015. ISSN 0004-637X. doi: 10.1088/0004-637X/806/1/20.

James Binney and Scott Tremaine. Galactic Dynamics: Second Edition. 2008.

James Binney, Ortwin Gerhard, and David Spergel. The photometric structure of the inner galaxy. Monthly Notices of the Royal Astronomical Society, 288:365–374, June 1997.

Ding Chen, Jing Huang, and Hong-Bo Jin. Spectra of Cosmic Ray Electrons and Diffuse Gamma Rays with the Constraints of AMS-02 and HESS Data. The Astrophysical Journal, 811:154, October 2015. ISSN 0004-637X. doi: 10.1088/0004-637X/811/2/154.

Walter Dehnen and James Binney. Mass models of the milky way. Monthly Notices of the Royal Astronomical Society, 294:429, March 1998.

T. Delahaye. Propagation of galactic cosmic rays and dark matter indirect detection. PhD thesis, LAPTH, Universit´e de Savoie, Universit´e de Savoie, July 2010.

D. R. Gies and J. W. Helsel. Ice age epochs and the sun's path through the galaxy. The Astrophysical Journal, 626:844–848, June 2005.

Ernst Hairer, Syvert Paul Nørsett, and Gerhard Wanner. Solving ordinary differential equations: Nonstiff problems. Springer, 1993. ISBN 9783540566700.

D. R. Lorimer. The galactic population and birth rate of radio pulsars. In F. Camilo and BM Gaenler, editors, Young Neutron Stars and their Environments, volume 218 of IAU Symposium, page 105, 2004.

Miyamoto and Nagai. Three-dimensional models fro the distribution of mass in galaxies. PASJ, 27: 533–543, 1975.

Bohdan Paczynski. A test of the galactic origin of gamma-ray bursts. The Astrophysical Journal, 348:485–494, January 1990.

B. Cameron Reed. The sun's displacement from the galactic plane from spectroscopic parallaxes of 2500 OB stars. Journal of the Royal Astronomical Society of Canada, 100:146, August 2006.

M. J. Reid and A. Brunthaler. The proper motion of sagittarius a*. II. the mass of sagittarius a*. The Astrophysical Journal, 616:872–884, December 2004.

Ralph Schönrich, James Binney, and Walter Dehnen. Local kinematics and the local standard of rest. Monthly Notices of the Royal Astronomical Society, 403:1829–1833, April 2010.

Nir J. Shaviv. Cosmic ray diffusion from the galactic spiral arms, iron meteorites, and a possible climatic connection. Physical Review Letters, 89:51102, 2002.

H. Svensmark. Imprint of galactic dynamics on earth's climate. Astronomische Nachrichten, 327: 866, November 2006.